Evaluating F2 region long term trends using the IRI model: A feasible approximation for experimental trends?

Bruno S. Zossi[1,2], Trinidad Duran[3,4], Franco D. Medina[1,2], Blas F. de Haro Barbas[1,2], Yamila Melendi[3,4], Ana G. Elias[1,2]

[1]INFINOA, CONICET-UNT, Tucuman, 4000, Argentina
[2]Laboratorio de Ionosfera, Atmosfera Neutra y Magnetosfera (LIANM), Facultad de Ciencias Exactas y Tecnología (FACET), Universidad Nacional de Tucumán (UNT), Tucuman, 4000, Argentina
[3]Departamento de Física, Universidad Nacional del Sur (UNS), Bahía Blanca, 8000, Argentina
[4]Instituto de Física del Sur (CONICET-UNS), Bahía Blanca, 8000, Argentina

Correspondence to: Ana G. Elias (aelias@herrera.unt.edu.ar)

Abstract. The International Reference Ionosphere (IRI) is a widely used empirical model of the ionosphere based on observations from a worldwide network of ionospheric stations. Therefore, it is reasonable to expect that it captures long-term changes in key ionospheric parameters, such as foF2 and hmF2 linked to trend forcings like greenhouse gases increasing concentration and the Earth's magnetic field secular variation. Despite the numerous reported trends in foF2 and hmF2 derived from experimental data and model results, there are persistent inconsistencies that require continuous refinement of trend estimation methods and regular data updates. This ongoing effort is crucial to address the inherent challenges posed by the weak signal-to-noise ratio associated with studying long-term trends in the ionosphere. Furthermore, the experimental verification of these trends remains challenging, primarily due to time and spatial coverage limitations of measured data series. Achieving these needs for long-term trend accurate detection requires extensive global coverage and resolution of ionospheric measurements together with long enough periods spanning multiple solar cycles to properly filter out variations of shorter term than the sought trend. Considering these challenges, IRI-modeled foF2 and hmF2 parameters offer a valuable alternative for assessing trends and obtaining a first approximation of a plausible global picture representative of experimental trends. This work presents these global trend patterns considering the period 1960-2022 using the IRI-Plas 2020 version, which are consistent with other model predictions. A verification was performed for foF2 trends, considering data from 9 mid-latitude stations, and a reasonable level of agreement was observed. It is concluded that IRI model can be a valuable tool for obtaining preliminary approximations of experimental trends.

1 Introduction

The International Reference Ionosphere (IRI) (Bilitza et al., 2022) is an empirical model based on observations from diverse sources. Therefore, it is reasonable to expect it to reflect, to some extent, the long-term trends observed in key ionospheric parameters such as the F2 region critical frequency, foF2, and the electron density peak height, hmF2. These trends, in

timescales of decades to a century, are theoretically expected as a consequence of trends in certain ionospheric forcings, such as the increasing greenhouse gases concentration and the Earth's magnetic field secular variation, among others (Lastovicka, 2017, 2021a).

35 There are countless foF2 and hmF2 reported trends based on experimental data, which combined with model results, led to a global scenario of trends with the main forcing being the increasing greenhouse gases concentration over the last decades (Lastovicka, 2017, 2021a). However, several inconsistencies remain to date that require a permanent update of data and refinement of the trend estimation methods in order to improve the signal-to-noise ratio that is extremely weak in the case of ionospheric long-term trends. Additionally, experimental verification is still far from being achieved mainly due to two

40 reasons: the limited time and spatial coverage of measured data series. The time span should cover at least two complete solar cycles to account for the primary ionospheric variability at these time scales. Filtering out this variability is essential for accurately detecting long-term trends. Moreover, the ionosphere presents other challenges that need extensive series in order to properly identify and analyze long-term trends. Regarding the spatial coverage, it should be global and with enough resolution so as to detect other forcings interfering with the expected trends whose intensity depend on location. This is the

45 case, for example, of Earth's magnetic field secular variation effect on the ionosphere which seems more prominent close to the geomagnetic equator (Cnossen, 2020; Elias et al., 2022). Given the difficulty of achieving these two requirements, we found it useful to evaluate trends from IRI modeled foF2 and hmF2 parameters and to analyze their usefulness as a reliable approximation of experimental trends.

Considering the global coverage of the IRI model, this research initially focuses on presenting the trends spanning the entire

50 planet. These trends are derived for the foF2 and hmF2 parameters, which are among the most significant ionospheric parameters (Cander, 2019). The calculation of these trends follows the same methodology applied to experimental data involving the simplest solar activity filtering approach. Furthermore, a comparative analysis is conducted between the trend values obtained from the IRI model and experimental trends in order to assess their accuracy. The continued refinement and updating of ionospheric trend estimation methods from data and models, together with data collection efforts, are essential for

55 improving our understanding of the underlying factors driving long-term changes in ionospheric parameters and their potential impacts on the diverse systems affected, such as communication and navigation systems.

This study is structured as follows: Section 2 provides an overview of the IRI model used. Sections 3 and 4 outline the methodology to derive global trends from IRI and to make a comparative analysis between these trends and experimental data across nine selected seasons, respectively. The results are presented in Section 5, followed by the discussion and conclusions

60 in Section 6, which includes a comparison with trends derived from other models.

2 On some aspects of the IRI model

The IRI is an observation-based climatological standard model of the ionosphere that is widely used for several purposes, including the prediction of ionospheric behavior useful for communication and global positioning systems (Gulyaeva and

Bilitza, 2012). The model is designed to provide vertical profiles of the main ionospheric parameters for any location over the globe, hours, seasons, and levels of solar activity, representing monthly mean conditions based on experimental evidence. Even though the improvement of the IRI representation of ionospheric parameters, including those selected in this study, still remains a challenge for the IRI Project, and despite its empirical nature and the potential for ongoing improvements, we choose to examine its suitability in estimating F2-region long-term trends, aiming to achieve the closest possible agreement with experimental trends.

Since its first edition in 1969 the IRI model has been steadily improved with newer data and with better mathematical descriptions of global and temporal variation patterns. A large number of independent studies have validated the IRI model in comparisons with direct and indirect ionospheric measurements not used in the model development (Gulyaeva and Bilitza, 2012; Bilitza et al., 2022).

In this study, we used an IRI adaptation, IRI-Plas that has been modified to include the plasmasphere, extending the model up to 20,000 km (Gulyaeva et al., 2011). While traditional IRI versions use fix solar activity proxies, such as IG for foF2, to estimate variations in ionospheric parameters associated to the solar activity quasi-decadal cycle, IRI-Plas allows selecting between different solar proxies, and among them the MgII index (core-to-wing ratio derived from the Mg II doublet at 280 nm). Since we choose this solar activity proxy for the filtering step before trend estimation, we decide to use this IRI version. The IRI-Plas model, from Izmiran (Moscow, Russia), was obtained from its online version available at https://www.izmiran.ru/ionosphere/weather/. According to IRI general specifications, we expect it to somehow force variations linked to changes in the geomagnetic field, since it uses the IGRF model to specify geomagnetic poles and equator, but not those variations expected from the increasing greenhouse gases concentration. Thus, our assumption is that trends occurring near the geomagnetic poles and equator, may not only arise from trends in experimental data, but could also be affected by forced adjustments resulting from IRI mathematical interpolation methods combined with the coupling to the geomagnetic field configuration. However, trends observed in other regions can be attributed exclusively to the experimental data.

3 Methodology to assess F2-region trends and spatial variation patterns based on IRI

To assess foF2 and hmF2 trends using IRI, monthly values were obtained first from IRI-Plas. This model was run over a 5°×10° latitude-longitude grid, covering 90°N to 90°S and 180°E to 180°W, along the period 1960-2022, specifically at 0 LT and 12 LT, with the following inputs: (1) MgII as the solar activity proxy, (2) CCIR maps for foF2, (3) storm model off. Considering just one day in the month or assessing the monthly median from all its daily values gives the same result due to IRI model presents a smooth variation at daily timescale. Therefore, we considered foF2 and hmF2 values for the 15th day of each month as equivalent to the monthly median.

A total of 37×37=1369 series were obtained for foF2 and for hmF2. In each case, annual mean series were constructed, together

95 with series for each of the 12 months (that is 13 series per grid point and per local time considered), all covering the period 1960-2022, which implies 63 points per series.

The foF2 and hmF2 filtering was made in the usual way, which is estimating the residuals from a linear regression between them and MgII as the solar EUV proxy (Lastovicka, 2021b, 2021c), according to:

$$X_{residual} = X_{IRI} - (A * MgII + B),$$ (1)

100 where XIRI is the IRI modeled foF2 or hmF2 data, and A and B are the least square parameters of the linear regression between XIRI and MgII. The linear trend was assessed from the linear regression between these residuals and time, that is

$$X_{residual} = \alpha t + \beta,$$ (2)

where t is in years and α is the desired trend in [MHz/year] in the case of foF2, or [km/year] in the case of hmF2. We will then have one α value for each grid point determining its worldwide variation, for the annual and the 12 monthly series. Global

105 means were calculated in each case using a cosine (latitude) weighting.

The selection of MgII as the solar proxy input for IRI-Plas, and to filter foF2 and hmF2 variability linked to solar activity, is based in recent studies which recommend the use of this index as a solar proxy for foF2 trend estimations (Lastovicka 2021b, 2021c; de Haro Barbas et al., 2021). We assume it is also the most adequate in the case of hmF2.

The MgII index was obtained from the University of Bremen. It is freely available at http://www.iup.uni-

110 bremen.de/UVSAT/Datasets/MgII (Viereck et al., 2010; Snow et al., 2014). The extended time series was considered in order to cover the period previous to 1978.

4 Methodology to evaluate the agreement between trends based on IRI and true experimental trends

Only foF2 was considered in the comparison between IRI and experimental trend values. In order to assess the level of agreement between model and data, 9 stations were chosen, which are listed in Table 1. foF2 trends at these stations were

115 evaluated using Eq. (1) to filter the solar activity effect and Eq. (2) to estimate trends in two ways: using the monthly median data, which will be called experimental trends (α_{exp}), and the IRI-Plas model output, which will be called IRI trends (α_{IRI}).

The following metrics commonly used in data-model prediction comparisons (Willmott and Matsuura, 2005; Chicco et al., 2021) were considered to compare IRI to experimental trends: the mean relative error (MRE) and the mean absolute error (MAE). Their equations are:

120 $$MRE = \frac{1}{n} \Sigma \frac{(\alpha_{IRI} - \alpha_{exp})}{\alpha_{exp}},$$ (3)

$$MAE = \frac{1}{n} \Sigma |\alpha_{IRI} - \alpha_{exp}|,$$ (4)

These parameters were assessed to compare overall IRI performance and its performance for each station. In the first case, summation is carried over the 9 stations considering the annual mean series, for 12 and 0 LT. In the second, summation is carried out for each station over the 12 months, also for 12 and 0 LT.

125

Table 1: Geographic coordinates and geomagnetic latitude of the 9 ionospheric stations analyzed to determine IRI foF2 trends accuracy.

Station	Geographic Latitude [°]	Geographic Longitude [°]	Geomagnetic Latitude [°]
Okinawa	26.31	127.59	17.28
Wakkanai	45.25	141.40	37.06
Kokubunji	35.71	139.49	27.28
Canberra	-35.17	149.08	-41.74
Townsville	-19.16	146.48	-26.21
Hobart	-42.53	147.19	-49.22
Juliusruh	54.60	13.40	53.98
Boulder	40.13	-105.23	47.65
Rome	41.54	12.29	41.49

MRE measures the average bias of IRI trends over or underestimating the experimental trends depending on its sign: positive
130 or negative, respectively. It gives similar information to the percentage bias, and its optimal value is 0. MAE is a scale-dependent measure of deviation that corresponds to IRI trends deviation from experimental ones. The optimal value of MAE is 0, indicating that both trends are identical.

Monthly median foF2 data from the ionospheric stations were obtained as follows. Japanese and Australian stations data are available from the National Institute of Information and Communications Technology, Japan
135 (https://wdc.nict.go.jp/IONO/index_E.html) and the World Data Centre (WDC) for Space Weather, Australia (https://downloads.sws.bom.gov.au/wdc/iondata/au/), respectively. Both databases contain monthly medians updated to 2022. European stations monthly medians up to 2009 were obtained from Damboldt and Suessman database (Damboldt and Suessman, 2012) (ftp://ftp.ips.gov.au/wdc-data/iondata/medians/Damboldt/). In the case of Juliusruh, the period was updated until 2022 with monthly medians available from https://www.ionosonde.iap-kborn.de/mon_fof2.htm. In the case of Boulder
140 and Rome the period was updated with data from Lowell GIRO Data Center (LGDC) (Reinisch and Galkin, 2011). foF2 from the Digital Ionogram Data Base (DIDBase) at LGDC has a frequency of 5 minutes. In order to obtain the monthly medians, we first selected data with Autoscaling Confidence Score (CS) greater than 70%, and then estimated for each month the hourly median. In the case of these three stations, it was checked that the last two years available from Damboldt and Suessman database had a reasonable coincidence (within 5%) with the data obtained from the other two sources.

5 Results

5.1 foF2 and hmF2 trends based on IRI model, and spatial variation pattern

Fig. 1 and 2 show foF2 and hmF2 trend values, respectively, for 12 LT and 0 LT. The geomagnetic equator is also plotted for years 1960 and 2022. foF2 trends are plotted in %, which were estimated by dividing α into foF2 mean along the complete period (1960-2022) at each grid point. In addition to overall negative trends in all cases, it can be noticed that the strongest trends occur in the region of the greatest geomagnetic equator displacement.

The global mean trends in each case are listed in Table 2, together with the mean values of F2-region parameters, to which the peak electron density, NmF2, was added in order to make some comparisons with other published results in the next Section. Trends are listed in absolute and percentage values. The squared correlation coefficient, r^2, of each parameter and MgII is also listed to indicate the quality of the fit to each regression model given by Eq. (1).

Table 2: Global mean values, using a cosine (latitude) weighting, of: F2-region ionospheric parameters, squared correlation coefficient (r2) of each parameter and MgII, linear trends of filtered parameters indicated in units per decade, and the same trends in percentage per decade.

	Mean	r^2	α	α [%/decade]
foF2(12 LT)	7.78 MHz	0.967	-0.10 MHz/decade	-1.31
foF2(0 LT)	4.87 MHz	0.962	-0.08 MHz/decade	-1.62
NmF2(12 LT)	8.05×10^5 cm^{-3}	0.970	-2.03×10^4 cm^{-3}/decade	-2.57
NmF2(0 LT)	3.18×10^5 cm^{-3}	0.963	-1.15×10^4 cm^{-3}/decade	-3.17
hmF2(12 LT)	303.1 km	0.959	-2.16 km/decade	-0.72
hmF2(0 LT)	323.0 km	0.971	-1.50 km/decade	-0.47

Trends assessed for each month have a similar spatial pattern as the annual trends shown in Fig.1, even though they are not identical. Fig. 2 (upper panel) shows the global mean trends values from January to December. Stronger global trends are noticed in February and in June. Something to notice is the decrease of r2 of the fit to filter solar activity, shown in Fig. 2 (upper panel). All values are lower than for the annual case. Evidently, solar proxies time series, when considered separately for each month, can explain less variance of ionospheric parameters variation, which in this case conserve variability patterns that are erased when annual means are used.

5.2 Agreement between IRI and experimental trends for selected stations

Fig. 3 and 4 show experimental and IRI foF2 trends for each of the 9 stations, at 12 and 0 LT, respectively, in terms of months. Error bars are estimated as two standard deviations. A general good agreement can be noticed, which is evinced by MAE and

170 MRE values listed in Table 3, in particular for the 12 LT case. Annual experimental and IRI trends are listed in Table 4, together with their errors (two standard deviations).

The cases with large MRE values correspond to those stations and LT that have an experimental trend value very close to zero. Since this value appears in the denominator of MRE (see Eq. 3), even a small difference in the numerator leads to a big MRE. However, we can re-estimate MRE's excluding experimental trends equal to zero within the error. Specifically, in the 12 LT

175 case, these would correspond to experimental trend values for Boulder in May; and in the 0 LT case, to Kokubunji in February and December, Townsville in June, Juliusruh in February, and Boulder in September and October. By doing so, the MRE decreases, as indicated by the values presented within brackets in Table 4.

Table 3: foF2 trends assessed with experimental data and with IRI-Plas model, considering annual mean data series at 12 and

180 0 LT. The last rows present the MAE and MRE between these trends considering the 9 stations. MRE* corresponds to MRE without the stations of highest relative error, that is Okinawa in the 12 LT case and Boulder in the 0 LT case.

Station	α [MHz/decade], 12 LT		α [MHz/decade], 0 LT	
	Experimental	IRI	Experimental	IRI
Okinawa	-0.30 ± 0.07	-0.14 ± 0.03	-0.18 ± 0.07	-0.18 ± 0.03
Wakkanai	-0.18 ± 0.05	-0.12 ± 0.03	-0.04 ± 0.02	-0.06 ± 0.01
Kokubunji	-0.20 ± 0.03	-0.13 ± 0.03	-0.07 ± 0.02	-0.09 ± 0.02
Canberra	-0.12 ± 0.04	-0.11 ± 0.02	-0.05 ± 0.03	-0.07 ± 0.02
Townsville	-0.16 ± 0.05	-0.13 ± 0.03	-0.09 ± 0.06	-0.10 ± 0.02
Hobart	-0.13 ± 0.04	-0.10 ± 0.02	-0.05 ± 0.03	-0.07 ± 0.02
Juliusruh	-0.11 ± 0.03	-0.11 ± 0.02	-0.06 ± 0.03	-0.06 ± 0.01
Boulder	-0.08 ± 0.06	-0.09 ± 0.03	0.01 ± 0.02	-0.04 ± 0.01
Rome	-0.13 ± 0.04	-0.12 ± 0.03	-0.10 ± 0.01	-0.08 ± 0.02
MAE	0.04 MHz/decade		0.03 MHz/decade	
MRE	-0.19 (-19%)		-0.79 (-79%)	
MRE*	-0.15 (-15%)		-0.16 (-16%)	

Table 4: MAE and MRE of foF2 trends assessed with experimental data and with IRI-Plas model, considering monthly data

185 series at 12 and 0 LT, for each station. MRE values between brackets correspond to estimation excluding experimental trends equal to zero within the error.

Station	α, 12 LT	α, 0 LT

	MAE [MHz/decade]	MRE	MAE [MHz/decade]	MRE
Okinawa	0.10	-0.39	0.05	0.27
Wakkanai	0.08	-0.35	0.02	-0.52
Kokubunji	0.06	-0.29	0.03	1.19 (0.28)
Canberra	0.02	-0.11	0.04	-0.48
Townsville	0.04	-0.10	0.04	-1.67 (-0.39)
Hobart	0.04	-0.23	0.02	0.50
Juliusruh	0.03	0.04	0.03	0.48 (-0.21)
Boulder	0.03	1.07 (0.51)	0.04	6.26 (0.21)
Rome	0.03	-0.08	0.04	0.26

6 Discussion and conclusions

We begin with a discussion of the agreement between the mean global trends obtained with IRI-Plas, as well as the spatial
190   variation of these trends, in comparison to other models. In particular, the Whole Atmosphere Community Climate Model
eXtension (WACCM-X) has been run with this purpose by Solomon et al. (2018) and by Cnossen (2020). The results that can
be compared are listed in Table 5.

In the case of Solomon et al. (2018), global mean values are presented considering only minimum solar activity level and solar
quiet conditions, with which no filtering is needed before the trend assessment. The period considered is 1972-2005, and there
195   is no local time consideration, so we will assume that their values could be compared to the mean of our 12 and 0 LT values.
Their trends are weaker than those assessed with IRI-Plas. In both cases trends are negative, but the NmF2 trend they obtain
is around half the IRI-Plas trend, as can be deduced from Table 5. In addition to trend values, NmF2 and hmF2 mean global
values estimated by Solomon et al. (2018) can be compared to IRI-Plas output averages considering only years around solar
minimum activity levels out of the 1960-2022 period. In this case, the results are similar for NmF2, but for hmF2 their mean
200   value is lower than that obtained with IRI-Plas.

Cnossen (2020) presents the global mean values, as in the previous case, and the spatial pattern variation. Our trend estimation
methodology is similar to Model 1 in this work, with two differences: F10.7 is used instead of MgII as solar proxy and the
trend term is included in a multiple regression together with the solar activity term. The differences due to methodologies is
not expected to be significant (Lastovicka et al., 2006). Trends in this case are slightly higher than in Solomon et al. (2018),
205   but again lower than those of IRI-Plas, with the greatest difference in NmF2 trend case, as can be noticed from Table 5. The
squared correlation coefficient, that indicates the quality of the fit to each regression model given by Eq. (1), is similar in all
the cases.

Table 5: Comparison between IRI-Plas and WACCM-X results from Solomon et al. (2018) and Cnossen (2020). All values correspond to global means along the period analyzed in each case, with the exception of NmF2 and hmF2 mean IRI-Plas values which correspond to global mean along solar minimum activity level periods.

	IRI-Plas (12 LT)	IRI-Plas (0 LT)	Solomon et al. (2018)	Cnossen (2020)
NmF2 trend [%/decade]	-2.6±0.8	-3±2	-1.2 %	-1.6±0.3
hmF2 trend [km/decade]	-2±1	-1.5±0.5	-1.3 km	-1.5±0.1
r^2(NmF2,MgII)	0.97	0.96	--	0.95
r^2(hmF2,MgII)	0.96	0.97	--	0.94
NmF2 mean [cm^{-3}]	2.14×10^5	1.39×10^5	1.74×10^5	--
hmF2 mean [km]	302.3	269.5	259.6	--

The spatial variation pattern can also be compared. In the case of hmF2, Cnossen (2020) spatial pattern is consistent with IRI-Plas trends at 12 LT, with overall negative trends and a positive patch above the geomagnetic equator between Africa and South America. This would be in agreement with the trend expected from the northward geomagnetic equator secular displacement, which is strongest in this region, and assuming that the equatorial ionization anomaly (EIA) pattern of hmF2 (highest values above the geomagnetic equator) moves along with this displacement. The highest decreasing trends are observed consequently below this positive patch, in response to the northward movement of hmF2 highest values. With respect to trend values, the strongest positive trends seem similar, around 2 km/decade. However, the highest negative trends are greatest in IRI-Plas case, reaching values of 12 km/decade at noontime while in Cnossen (2020) case this value corresponds to 5 km/decade.

In the case of hmF2 trends at 0 LT, hmF2 presents a valley, even though not as well defined as the crest during daytime hours. The displacement of this valley attached to the geomagnetic field northward displacement induces an effect inverse to that during noon. That is a positive trend patch appears below it, with the strongest negative trends above.

A similar situation occurs with foF2 trend spatial pattern. In order to compare the trend values in percent with those of NmF2, they should be multiplied by two. This means that our strongest negative trend is again the highest. The spatial pattern here has alternating bands of positive and negative trend values aligned with the EIA, which can be explained in terms of the EIA displacement following the geomagnetic equator. Between ~60°W and 0° in longitude the equator shift is the greatest and northward, so this is the region where the strongest alternating trends are noticed (Elias et al., 2022). This longitudinal extension is narrower than in Cnossen (2020) case, who detect it between ~60°W and ~20°E. A notorious difference is that between the initial and the final position of the geomagnetic equator in this longitudinal range, Cnossen (2020) detects a negative trend band while in our case a positive band is observed.

This difference may be caused by a poor resolution in latitude. In order to see the trend bands expected in the region between
235 the initial and final position of the equator, a schematic plot is shown in Fig. 5(a) of the EIA foF2 valley in its initial and its
final position in 1960 and 2022, respectively. In this figure, it can be clearly noticed that the region between these positions
will present a positive portion followed by a negative one. The first one corresponds to the region with low foF2 in 1960,
which has now become a region with higher foF2 values (since the valley has moved). The second one corresponds to a region
of higher foF2 in 1960, which now is located under the EIA valley (since the valley has approached). On average, the
240 geomagnetic equator has displaced ~5 to 10° in the region's strongest shift, so for low resolutions, the grid points may coincide
with one of either trend bands. This could partly explain the difference between Cnossen (2020) negative band between the
equator positions, and our corresponding positive band. Fig. 5(b) shows an enlarged portion of the trends spatial pattern
obtained with IRI-Plas, but increasing the latitude resolution to 1°, where it can be noticed a positive and a negative band
within the limits of the 1960 and the 2022 equator positions.

245 The spatial pattern linked to the EIA displacement following the geomagnetic equator, is expected in IRI-Plas foF2 and hmF2
modeling since the model includes a real geomagnetic field and, even though there are very few stations along its location, IRI
model reproduces the EIA pattern. The overall negative trends in both, foF2 and hmF2, is in agreement with that expected
from increasing greenhouse concentration. Taking into account that IRI model does not include any forcing linked to these
gases, the trends observed can be attributed to the data.

250 To verify this, we have compared foF2 and hmF2 trends, considering annual and monthly series, obtained with experimental
data obtained from 9 mid-latitude stations and with the corresponding IRI-Plas modeled values. We obtained a reasonable
agreement, with average differences of ~20%. Something to argue is that by using mid-latitude stations, we use the stations
for which IRI surely works best. Therefore, an important pending task would be to make this comparison with low and high
latitude stations. Another pending task is to extend the comparison to hmF2 case.

255 It is important to remark that IRI-Plas is an ionospheric model while WACCM-X is a general circulation model. IRI is
continuously updated, using stations data to represent the ionosphere, it is easy to use and can be run in modest computers
consuming few resources. On the other hand, IRI adopts simplified assumptions and parameterizations to represent complex
ionospheric processes in order to consume less computational time, making it a reliable tool to get an approximated status of
the ionosphere.

260 WACCM-X is a complex model with high-resolution modeling capabilities, which incorporate a comprehensive set of physics
processes to estimate a more realistic representation atmospheric (and ionospheric) status, including chemical, dynamical, and
radiative processes. This model is coupled with several Earth systems, making easy to analyze the weight of any change in
trends, e.g. the increase of a particular component in atmospheric composition. Nevertheless, the negative side of general
circulation models is the substantial computational resources and time needed to run simulations, being almost exclusive for
265 high-performance computing centers.

Given the results presented in this study, we conclude that IRI-Plas can be a valuable tool for obtaining preliminary
approximations of experimental trends, at least in the case of foF2. This is particularly significant given the low spatial density

of data and the scarcity of series with sufficient length to estimate trends. In the case of hmF2, there would be an added advantage considering that, while foF2 is an accurately measured parameter, hmF2 is often missing or represented by the proxy

270 M(3000)F2 parameter.

Competing interests

The contact author has declared that none of the authors has any competing interests.

Acknowledgements

B.S. Zossi, F.D. Medina, B.F. de Haro Barbas and A.G. Elias acknowledge research project PIP 2957. T. Duran acknowledge
275 research projects PICT 2019-03491 and PGI 24/F083.
We acknowledge GIRO data resources http://spase.info/SMWG/Observatory/GIRO, and IONOLAB (www.ionolab.org/) for providing IRI Plas software.

References

Bilitza, D., Pezzopane, M., Truhlik, V., Altadill, D., Reinisch, B. W., and Pignalberi, A.: The International Reference
280 Ionosphere model: A review and description of an ionospheric benchmark, Reviews of Geophysics, 60, e2022RG000792, doi:10.1029/2022RG000792, 2022.

Cander, L. R.: Space Weather Causes and Effects. In: Ionospheric Space Weather. Springer Geophysics. Springer, Cham, 29-58, doi:10.1007/978-3-319-99331-7_3, 2019.

Chicco D., Warrens M.J., and Jurman G.: The coefficient of determination R-squared is more informative than SMAPE, MAE,
285 MAPE, MSE and RMSE in regression analysis evaluation, PeerJ Computer Science, 7, e623, doi:10.7717/peerj-cs.623, 2021.

Cnossen, I.: Analysis and attribution of climate change in the upper atmosphere from 1950 to 2015 simulated by WACCM-X, J. Geophys. Res., 125, e2020JA028623, 2020.

Damboldt, T. and Suessmann, P.: Consolidated Database of Worldwide Measured Monthly Medians of Ionospheric Characteristics foF2 and M(3000)F2. INAG (Ionosonde Network Advisory Group) Bulletin 73
290 https://www.ursi.org/files/CommissionWebsites/INAG/web-73/2012/damboldt_consolidated_database.pdf, 2012.

de Haro Barbas, B. F., Elias, A. G., Venchiarutti, J. V., Fagre, M., Zossi, B. S., Tan Jun, G., and Medina, F. D.: MgII as a Solar Proxy to Filter F2-Region Ionospheric Parameters, Pure Appl. Geophys. 178, 4605–4618, doi:10.1007/s00024-021-02884-y, 2021.

Elias, A. G., de Haro Barbas, B. F., Zossi, B.S., Medina, F. D., Fagre, M., and Venchiarutti, J. V.: Review of Long-Term

295 Trends in the Equatorial Ionosphere Due the Geomagnetic Field Secular Variations and Its Relevance to Space Weather,

Atmosphere, 13, 40, doi:10.3390/atmos13010040, 2022.

Gulyaeva, T. and Bilitza, D.: Towards ISO Standard Earth Ionosphere and Plasmasphere Model, New Developments in the

Standard Model, Ed. R.J. Larsen, Nova Science Publishers, New York, 2012.

Gulyaeva, T.L., Arikan, F. and Stanislawska, I.: Inter-hemispheric imaging of the ionosphere with the upgraded IRI-Plas model

300 during the space weather storms, Earth Planet Sp 63, 929–939. doi:10.5047/eps.2011.04.007, 2011.

Laštovička, J., Mikhailov, A.V., Ulich, T., Bremer, J., Elias, A.G., Ortiz de Adler, N., Jara, V., Abarca del Rio, R., Foppiano,

A. J., Ovalle, E., Danilov, A.D.: Long-term trends in foF2: A comparison of various methods, Journal of Atmospheric and

Solar-Terrestrial Physics, 68(17), 1854–1870. doi:10.1016/j.jastp.2006.02.009, 2006.

Lastovicka, J.:A review of recent progress in trends in the upper atmosphere, J. Atmos. Solar-Terr. Phys., 163, 2–13,

305 doi:10.1016/j.jastp.2017.03.009, 2017.

Lastovicka, J.: Long-Term Trends in the Upper Atmosphere, in Upper Atmosphere Dynamics and Energetics; Wang, W.,

Zhang, Y., Paxton, L.J., Eds.; American Geophysical Union: (Washington D.C.) USA, 325–344, 2021a.

Lastovicka, J.: What is the optimum solar proxy for long-term ionospheric investigations? Adv. Space Res., 67, 2-8.

doi:10.1016/j.asr.2020.07.025, 2021b.

310 Lastovicka, J.: The best solar activity proxy for long-term ionospheric investigations, Adv. Space Res., 68, 2354-2360,

doi:10.1016/j.asr.2021.06.032, 2021c.

Reinisch, B.W. and Galkin, I.A.: Global ionospheric radio observatory (GIRO), Earth Planets and Space 63: 377-381,

doi:10.5047/eps.2011.03.001, 2011.

Snow, M., Weber, M., Machol, J., Viereck, R., and Richard, E.: Comparison of Magnesium II core-to-wing ratio observations

315 during solar minimum 23/24, Journal of Space Weather and Space Climate, 4, A04. doi:10.1051/swsc/2014001, 2014.

Solomon, S. C., Liu, H.-L., Marsh, D. R., McInerney, J. M., Qian, L., and Vitt, F. M.: Whole atmosphere simulation of

anthropogenic climate change. Geophys. Res. Lett., 45, 1567–1576. doi:10.1002/2017GL076950, 2018.

Viereck, R. A., Snow, M., DeLand, M. T., Weber, M., Puga, L., and Bouwer, D.: Trends in solar UV and EUV irradiance: An

update to the Mg II Index and a comparison of proxies and data to evaluate trends of the last 11-year solar cycle, Abstract

320 GC21B-0877 presented at 2010 Fall Meeting, AGU, San Francisco, CA, 13-17 Dec, 2010.

Willmott, C.J. and Matsuura, K.: Advantages of the mean absolute error (MAE) over the root mean square error (RMSE) in

assessing average model performance, Climate Research, 30, 79–82. doi:10.3354/cr030079, 2005.
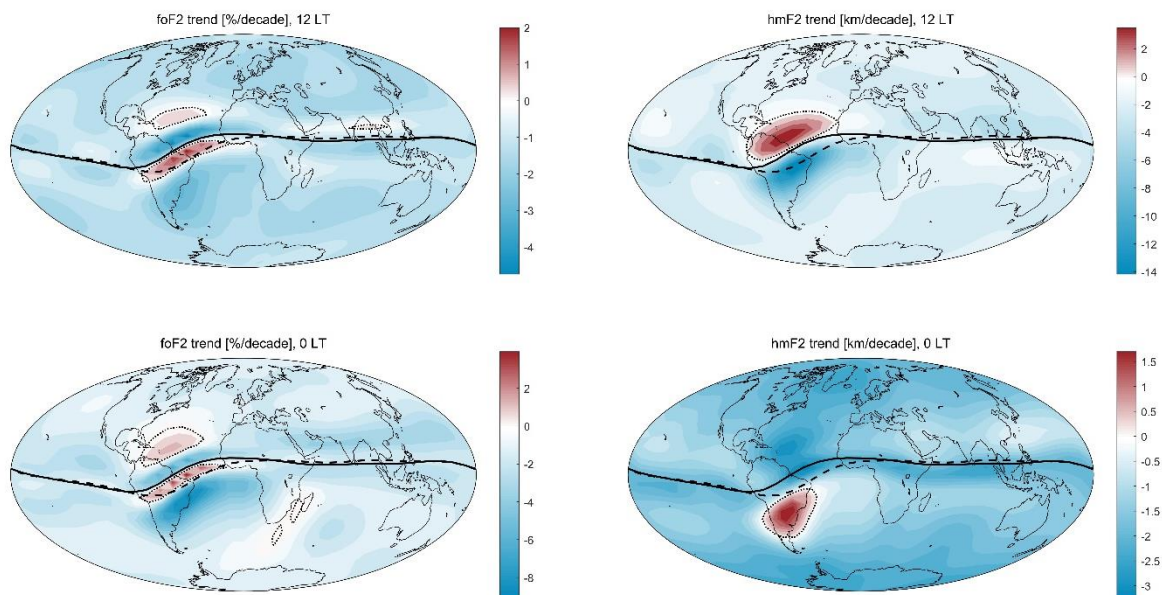
Figure 1: Trends of foF2 (left panels) and hmF2 (right panels), at 12 LT (upper panels) and 0 LT (lower panels) along the period 1960-2022 assessed with IRI outputs, which were previously filtered using Eq. (1). Note: Trends are indicated per decade, and foF2 trends are in percent. Enhanced dashed and solid lines indicate the magnetic equator position in 1960 and in 2022, respectively. Dotted lines indicate zero trend.
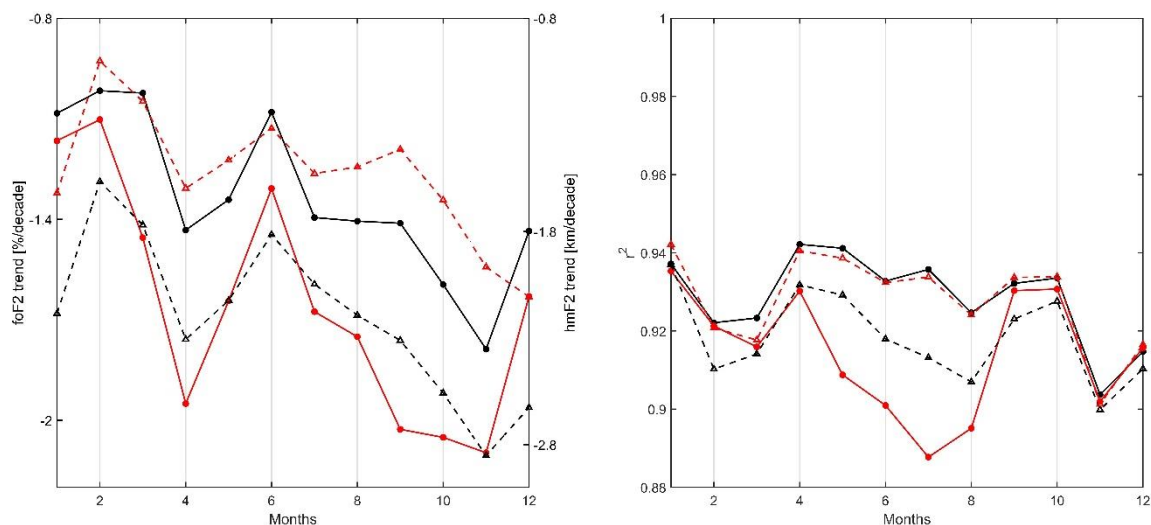
Figure 2: Global mean values of the linear trends (left panel) and the squared correlation coefficient (r2) between each parameter and MgII (right panel) of foF2 (solid line with circles) and hmF2 (dashed lines with triangles) at 12 LT (in black) and 0 LT (in red).
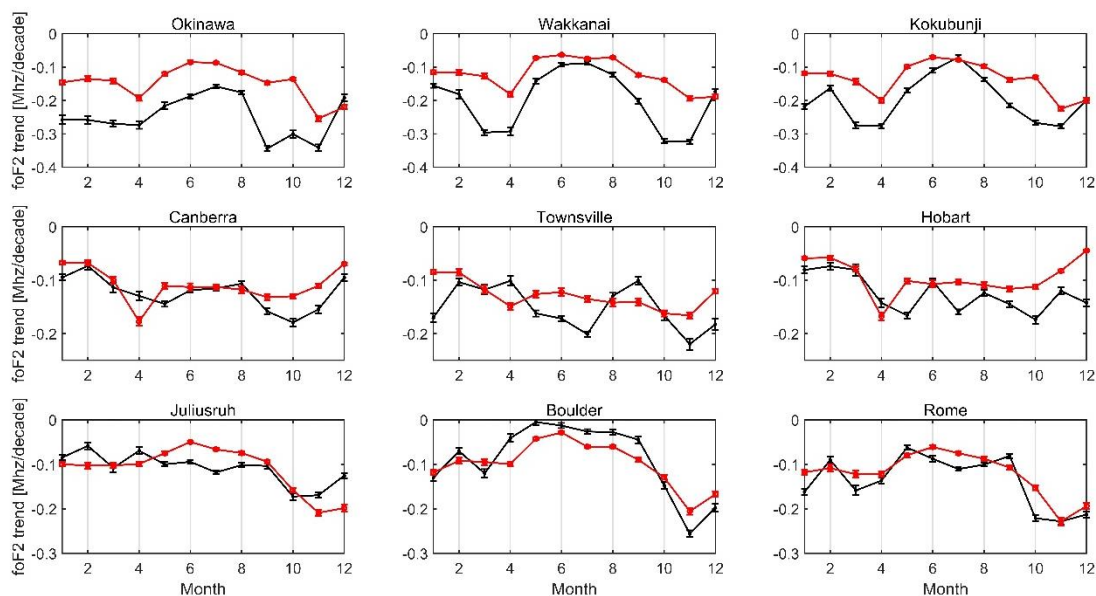
335

Figure 3: Monthly variation of foF2 trends in [MHz/decade], at 12 LT, estimated with experimental data (black) and with IRI-Plas model (red). Error bars correspond to two standard deviations.
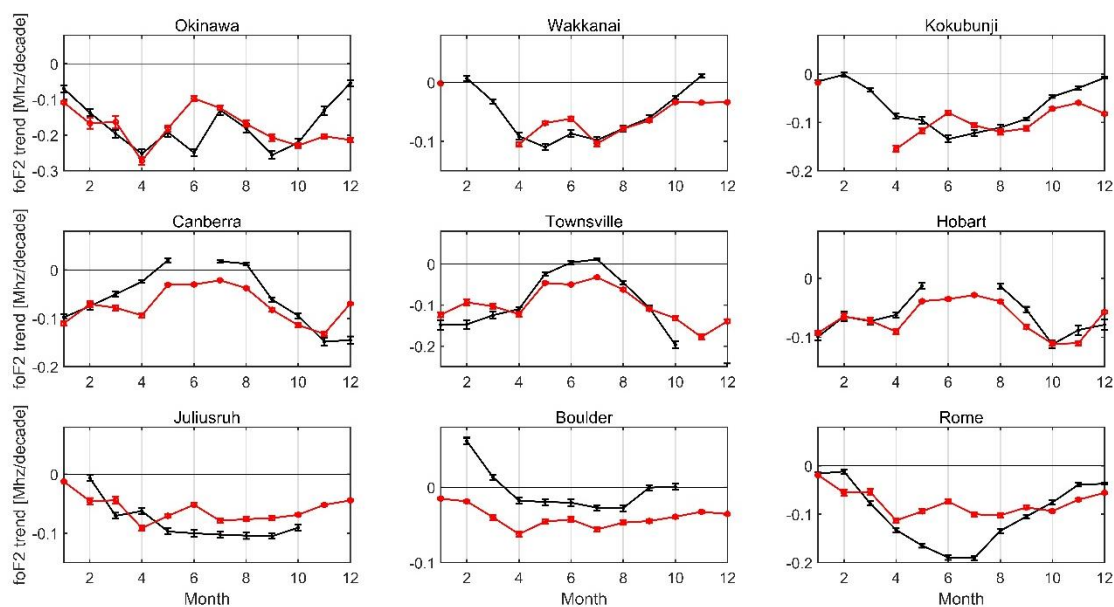
340   **Figure 4: Monthly variation of foF2 trends in [MHz/decade], at 0 LT, estimated with experimental data (black) and with IRI-Plas model (red). Error bars correspond to two standard deviations.**
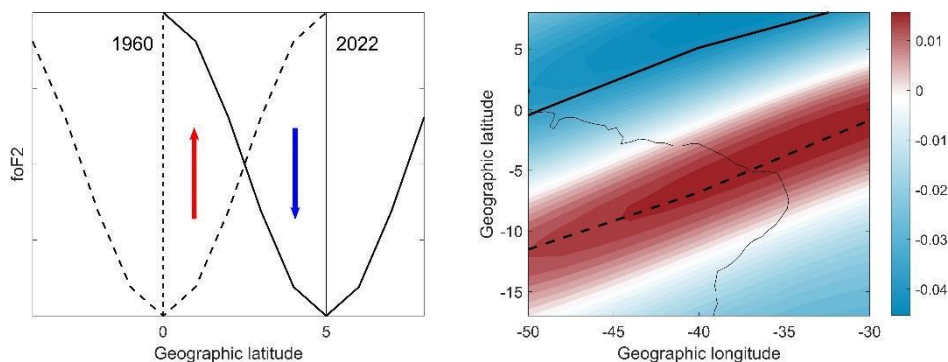
Figure 5: (Left panel) Schematic representation of foF2 latitudinal profile around the EIA valley in 1960 (dashed line), centered in the magnetic equator in 1960 (vertical dashed line at latitude=0), and in 2022 (solid line), centered in the magnetic equator in 2022 (vertical solid line at latitude =5). The red arrow indicates the foF2 increase that would be observed in latitudes between 0 and ~2.5, and the blue arrow the decrease between ~2.5 and 5. (Right panel) foF2 trend along 1960-2022 assessed with IRI-Plas (solar activity filtering with MgII) in the region with the largest equator displacement with an increased resolution: 1°×2° latitude-longitude grid. Enhanced dashed and solid lines indicate the magnetic equator position in 1960 and in 2022, respectively.